Journal of Materials Chemistry A

ROYAL SOCIETY OF CHEMISTRY

PAPER

View Article Online
View Journal | View Issue

Cite this: J. Mater. Chem. A, 2026, 14, 16510

Conformational isomerism tunes barocaloric potential of MIL-53(Ga)-fum frameworks

C. C. Hong, [a] W. L. W. Leung,[b] C. Wilson, [b] M. J. Liddle,[b] R. S. Forgan, [b] J. J. B. Levinsky, [a] A. S. J. S. Mey [a] and C. L. Hobday *[a]

With the negative implications of current refrigerants on the environment, there is a necessity for greener alternatives. Solid-state caloric materials exhibit large entropy and temperature changes that avoid liquid-vapour transitions of current refrigerants. Through guest adsorption, flexible metal-organic frameworks (MOFs) exhibit large entropy changes under small applied pressures, making them promising candidates. Though effective, flexible MOFs lack long-term mechanical stability owing to the mechanical stress induced during operation. Herein, we highlight and categorise the previously unexplored conformational isomerism of the MIL-53(X)-fum frameworks, which originates from the relative orientations of the fumarate linkers, and explore the effect on structural flexibility and barocaloric potential. Using single crystal X-ray diffraction (SCXRD) and *ab initio* molecular dynamics (AIMD), we reveal the third and final possible conformational isomer, MIL-53(X)-fum(*c*), to complement the two previously reported (MIL-53(X)-fum(*a*) and MIL-53(X)-fum(*b*)), and investigate the effects of the isomerism on the framework properties. We uncover the isomerically unique mechanical stability of MIL-53(Ga)-fum(*c*) through simulated potential energy surfaces and find that the vacated open phase has exceptional thermal stability of up to 650 K. Through grand canonical Monte Carlo (GCMC) simulations, the reversible adsorption-driven entropy changes under 0.4 MPa of applied pressure were calculated to be ΔS = 210(30) J K^{-1} kg^{-1} and 150(30) J K^{-1} kg^{-1} for the adsorption of H_2O and CO_2, respectively. The results of our studies suggest that MIL-53(Ga)-fum(*c*) can exhibit a caloric response that is competitive with current commercial refrigerants. Furthermore, we outline the significance of exploring conformational isomerism in MOFs to increase the space in which materials discovery can occur.

Received 3rd November 2025
Accepted 17th March 2026

DOI: 10.1039/d5ta08920d

rsc.li/materials-a

Introduction

The continuous increase of the average global temperature makes the effects of climate change apparent and results in an increased demand for refrigeration in everyday life.[1] This is reflected by the projected growth of the global refrigerator market size from $74.74 billion to $120.01 billion between 2023 to 2032.[2] Currently, refrigeration is primarily achieved by the vapour compression cycle of gaseous refrigerants such as hydrofluorocarbons (HFCs), shown in Fig. 1a.[3] HFCs have large global warming potentials (GWP) and, therefore, contribute significantly to climate change.[1,4] Hence, there is an urgent need to identify sustainable alternatives.

A promising way of addressing this issue is to use a solid-state caloric approach which eliminates the need for a gas-liquid phase change. The caloric effect is defined as the induced temperature change under an externally applied field.[5] The application of magnetic fields, electric fields, uniaxial stress, or hydrostatic pressure gives rise to the magnetocaloric, electrocaloric, elastocaloric, and barocaloric effects, in turn.[6] An example of a solid-state cooling cycle based on the barocaloric effect is shown in Fig. 1b. For calorics to be viable for refrigeration applications, their performance must be comparable or better than the HFCs. The performance of a caloric material is quantified by the isothermal entropy change (ΔS_{iso}), adiabatic temperature change (ΔT_{ad}), and the field required to drive the transition, for example, the change in hydrostatic pressure (ΔP).[7] A commonly used HFC, R-134a (1,1,1,2-tetrafluoroethane), exhibits an ΔS_{iso} = ~520 J kg^{-1} K^{-1} for ΔP = 1.5 MPa.[8,9] Specific interest was garnered towards barocaloric materials when Li *et al.* and Lloveras *et al.* demonstrated that neopentyl glycol (NPG) exhibits pressure-driven entropy changes on par with R-134a.[10,11]

There are three main challenges associated with barocalorics. (1) The working pressure (ΔP) required to drive the phase transition is typically large. For practical applications, the ΔP required should ideally be lower than 30 MPa as set out by the Henry Royce Institute.[12] (2) The isothermal entropy change (ΔS_{iso}) must be comparable to, or improve on, that of current

[a]EaStCHEM, School of Chemistry and Centre for Science at Extreme Conditions, University of Edinburgh, Edinburgh, UK. E-mail: claire.hobday@ed.ac.uk
[b]School of Chemistry, University of Glasgow, Glasgow, UK. E-mail: ross.forgan@glasgow.ac.uk

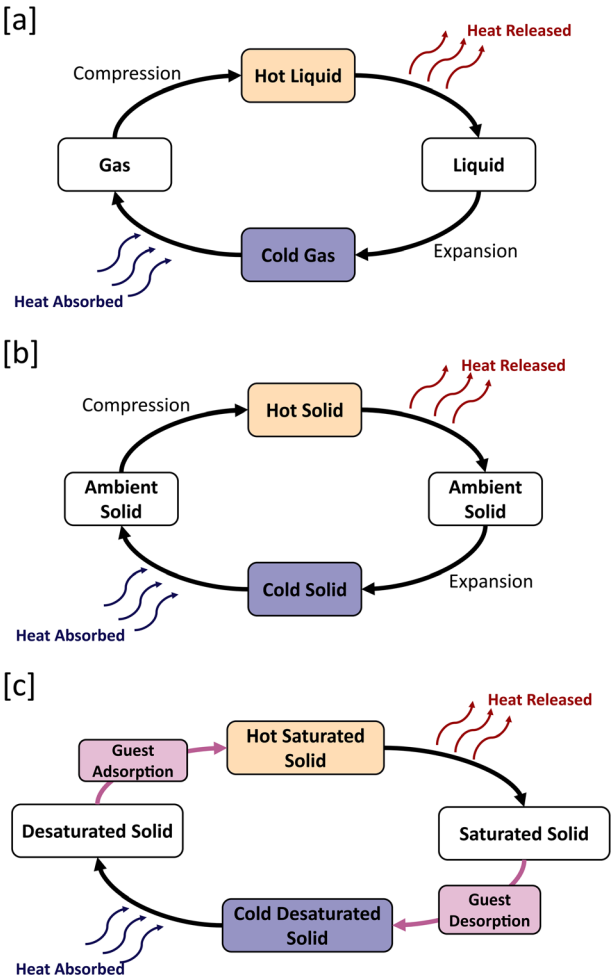

Fig. 1 Schematic of different refrigeration cycles. (a) A vapour compression cycle where the phase of the material relative to the liquid–vapour phase boundary can be controlled with compression or decompression of the material. (b) A solid-state barocaloric cycle. Driven by hydrostatic pressure, the refrigerant undergoes a solid–solid phase change which result in the absorption or emission of heat into the surrounding. (c) An adsorption driven refrigeration cycle where the temperature change is induced by the adsorption of gaseous guest molecules onto or into the solid material.

refrigerant gases. (3) The mechanical stress induced during cyclic operation by repeated large volume changes (ΔV) can lead to mechanical failure. This is commonly observed in temperature- or pressure-induced structural phase transitions which give rise to the formation of defects that alter the properties of crystalline materials.[13–15] While a variety of material systems such as molecular and ionic plastic crystals,[16,17] spin-crossover compounds,[18] inorganic salts,[19] and two-dimensional perovskites[20] have been reported to exhibit colossal barocaloric effects, the ΔP values required to drive such responses are still preventively high. Metal-organic frameworks (MOFs) are a class of caloric materials which have demonstrated the ability to operate at pressures in the same magnitude as that of R-134a.[8,21]

MOFs are a class of porous, crystalline materials consisting of metal nodes that are coordinated by organic linkers, which extend to create a framework that is highly modular in structure and properties.[22–24] Their versatility and tuneable properties mean these materials have found applications across various fields such as gas storage,[25–28] drug delivery,[29] molecular sieves for mixture separations,[30,31] substrate specific catalysis,[32,33] and many more.[34–36] Many MOFs have intrinsically flexible topologies, exhibiting significant structural changes in response to external stimuli such as temperature, pressure, and the presence of pore-bound guests.[37,38] This feature has been coined "breathing" and is generally attributed to several factors such as inherent ligand flexibility, metal polarization, and degrees of freedom within the framework topology.[39–41] These easily accessible, large amplitude volume changes and gas adsorption processes make MOFs potential candidates as caloric materials. The working mechanism is similar to barocalorics but instead of non-penetrating hydrostatic pressure, penetrating gaseous pressure is applied which leads to gas adsorption and drives the phase transition, hence the term "breathing-calorics".[8] An example of this adsorption-driven cooling cycle is shown in Fig. 1c.

In 2022, García–Ben *et al.* reported an $\Delta S_{iso} = 311$ J K^{-1} kg^{-1} by the application of 1.6 MPa of carbon dioxide pressure to the flexible MOF, MIL-53(Al) (MIL = Matériaux de l'Institut Lavoisier). The structure of MIL-53(Al) is characterised by one-dimensional $[Al(RCO_2)_2(OH)]_n$ chains that are bridged by μ_2-OH units and 1,4-benzenedicarboxylate (BDC) linkers.[8] Induced by temperature changes or by the adsorption and desorption of carbon dioxide molecules, MIL-53(Al) undergoes "open-to closed-pore" structural phase transitions with $\Delta V = 50\%$.[42,43] With such a large ΔV, the problem with mechanical failure remains. Following this, carbon dioxide adsorption in MOF-508b ($[Zn_2(BDC)_2(bpy)]$, bpy = 4,4′-bipyridine) was studied.[21] MOF-508b exhibits a two-step structural phase transition with $\Delta V_1 = 14.4\%$ and $\Delta V_2 = 3.8\%$ that is accompanied by a total $\Delta S_{iso} = 438.0$ J K^{-1} kg^{-1}. Despite the smaller overall ΔV, the ΔS_{iso} was larger than that of MIL-53(Al). Pressure-gradient differential scanning calorimetric (PGDSC) studies by Feldmann *et al.* showed that the ΔS_{iso} from the ΔV was endothermic in nature as opposed to the exothermic ΔS_{iso} that arises from the corresponding adsorption event.[44] Thus, it was concluded that minimising the ΔV could not only reduce mechanical failure, but also increase the overall ΔS_{iso}, that is primarily due to gas adsorption. In this work, we therefore explore rigid MOFs, which show minimal volume change ($\Delta V \approx 0\%$) during adsorption–desorption cycles, as potential refrigerants. While previous studies have mainly addressed the caloric effects of flexible MOFs or the gas capture properties of rigid MOFs,[21,26,29,45,46] our work connects these two domains.

MIL-53(X)-fum (X = Al, Ga, In, and fum = fumarate) is an isoreticular analogue to the archetypal MIL-53(X) framework with the fumarate dianion, derived from (2*E*)-but-2-enedioic acid, replacing BDC as the organic linker. The structure of the Al homologue, commercialised by BASF as Basolite A520, was not reported until 2015 despite significant early investigations into its adsorption capabilities.[47] The crystal structure of hydrated MIL-53(Al)-fum was obtained by a combination of analyses, including solid-state NMR spectroscopy, powder X-ray diffraction, and molecular simulations.[48] The Ga homologue

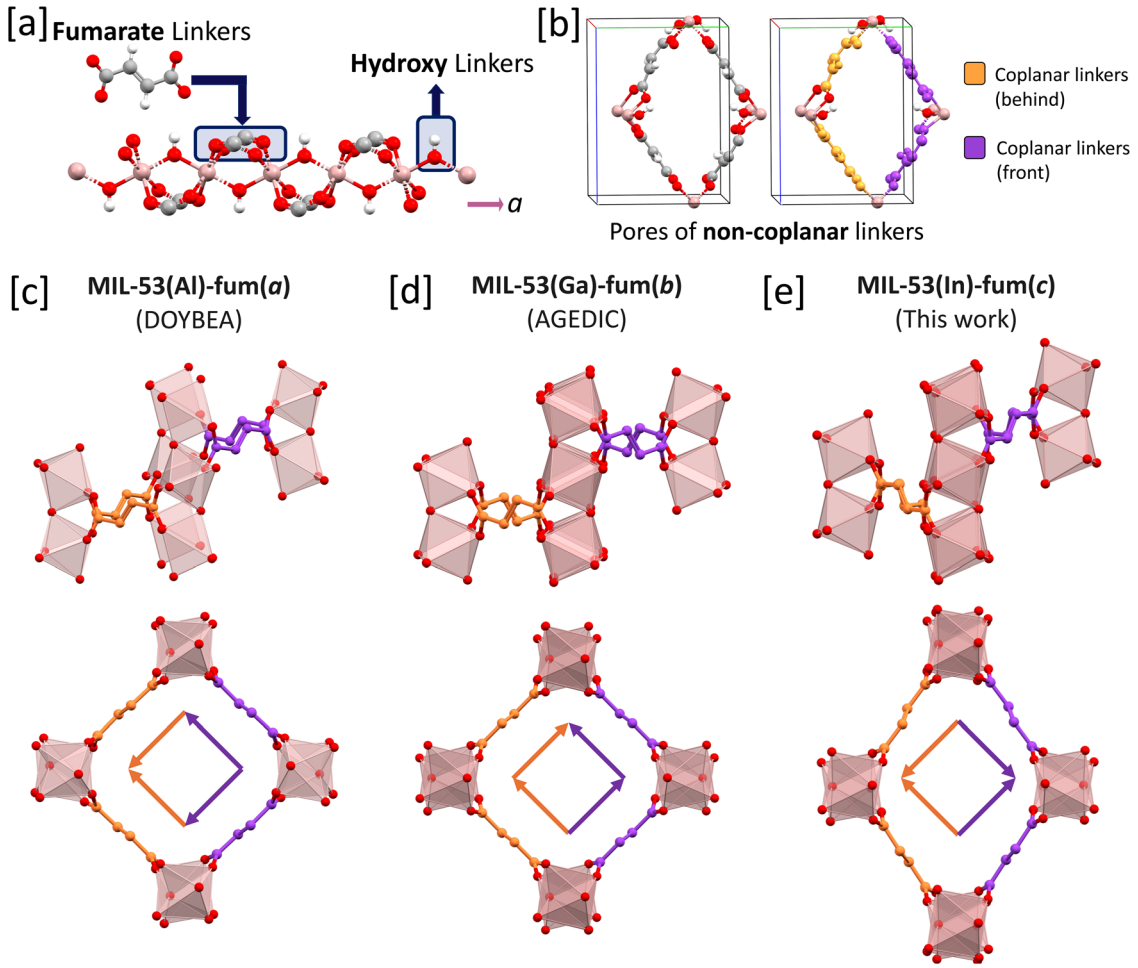

Fig. 2 Non-coplanar nature and classification scheme of the MIL-53(X)-fum frameworks. (a) The one-dimensional chains of metal oxide nodes along the *a*-direction with the oxygens from either the fumarate or hydroxyl linkers. In this representation, the colours: red, white, grey, and pink denote the elements: oxygen, hydrogen, carbon, and metal, respectively. (b) The porous environment is shown by observing the structure on the *bc*-plane. In this plane, it is noted that the four linkers around a pore are not all coplanar but rather, form coplanar pairs, as highlighted by the orange and purple colours. (c)–(e) Crystal structures and vector diagrams showing the three possible local structures based on fumarate disorder where (c) is MIL-53(Al)-fum(*a*) (DOYBEA),[47] (d) is MIL-53(Ga)-fum(*b*) (AGEDIC),[49] and (e) is MIL-53(In)-fum(*c*) (from this work). The first row shows the side view of the pores highlighting which of the fumarate linkers are coplanar (based on orange/purple colour scheme). The side view also highlights the differences in linker orientation between the different conformational isomers. The structures in the second row show the front view of the framework pores, maintaining the same colour scheme as before. From this, we derive the vector diagrams seen inside the pores where the direction of the arrows denotes the orientation of the linker as "up" or "down". When travelling in the direction of the arrow, one would go "downhill" across the C=C double bond in the centre of the fumarate linker.

was reported soon after.[49] The powder X-ray diffractogram was said to strongly resemble that of Basolite A520 and thus, density functional theory (DFT) optimisation was used to derive the structure of MIL-53(Ga)-fum from that of the Al homologue, yielding the hydrated and anhydrous MIL-53(Ga)-fum framework structures. This study of the mechanical response of MIL-53(Ga)-fum concluded that it shows promise as a "shock absorber" for mechanical energy storage. Around the same time, a separate study reported the syntheses of the Ga and In homologues, including a crystal structure of hydrated MIL-53(Ga)-fum determined by Rietveld refinement which showed subtle differences to the previous MIL-53(Ga)-fum structure.[50]

A key missing element from the studies conducted on these homologues is the consideration of the inherent asymmetric nature of the fumarate linker. Despite the isoreticular nature of the various reported MIL-53(X)-fum frameworks, we note distinct variances in terms of the fumarate linker orientations. We denote these different structures as conformational isomers. Our analyses of the structures of MIL-53(Ga)-fum, studied by Ramaswamy *et al.*, and the Al Basolite A520 have determined they comprise the same isomer.[47,49] On the other hand, the MIL-53(Ga)-fum solved by Zhang *et al.* exists as a different conformational isomer.[50] In this work, we have synthesised and experimentally characterised what we believe to be the first confirmed single crystal structure of a third isomer of MIL-53(X)-fum. While this isomer has yet to be reported for fumarate-based frameworks, we have identified this conformational isomer in the structure of the related MOF,

MIL-53(Al)-mes (mes = mesaconate, a mono-methylated derivative of fumarate), which was obtained using Rietveld refinement by Stassin *et al.*[51] Notably, conformational isomers of MOFs based on linker orientation have been known to exhibit distinctive properties. Examples include DUT-8, TRUMOF-1, and IRMOF-3-AMPh which showed different closing mechanisms, mechanical properties, and elastic stability, respectively.[52–54] Hence, the identification and understanding of the properties of these conformational isomers are significant.

In a previous study by S. Ehrling *et al.* a simple schematic to describe linker-based disorders was conceived, where each porous environment was represented as a jigsaw piece and the edges represented the orientation of the linker.[55] This cannot be translated to the MIL-53(X)-fum series due to the one-dimensional chains of the MIL-53 framework structure (see Fig. 2a); the four linkers making up the pore are not all coplanar to each other (see Fig. 2b).[56] The similarities and distinctive differences between the three isomeric structures are exemplified in Section 2 of the SI, highlighting the difficulties in discerning between the structures and the need for a simplified presentation. We have therefore devised a scheme based on a vector diagram to differentiate between the conformational isomers (see Fig. 2c, d, and 2e). The colour of the arrows encode information on which fumarate linkers are coplanar, *i.e.*, connect the same two metal ions on the one-dimensional chain secondary building unit (SBU). The direction of the arrow indicates the orientation of the linker, travelling upwards or downwards in connecting two chain SBUs. The different conformational isomers (Fig. 2c–e) will be denoted as MIL-53(X)-fum(*a*/*b*/*c*), hereafter.

Based on this scheme, we can classify the structures of MIL-53(Ga)-fum reported by Ramaswamy *et al.,* and the original report of MIL-53(Al)-fum (Basolite A520), to be of the isomer, MIL-53(X)-fum(*a*).[47,49] We then find the Ga homologue reported by Zhang *et al.* to correspond to the MIL-53(Ga)-fum(*b*) conformational isomer.[50] The MIL-53(In)-fum single crystal structure obtained in this study (*vide infra*) comprises the third isomer, MIL-53(In)-fum(*c*), which adopts the same conformation as the related structure of MIL-53(Al)-mes reported by Stassin *et al.*[51] Based on our schematic, this final isomer completes the set of possible conformational isomers stemming from the relative orientations of the fumarate linkers within this particular topology.

Experimentally, there are various challenges associated with the structure determination of these isomers of MIL-53(X)-fum. Firstly, difficulties in obtaining single crystals suitable for X-ray diffraction have necessitated the use of powder X-ray diffraction to date, generating data which, in theory, could be sensibly refined to obtain any of the isomers depending on the methods used. In addition, the presence of individual crystals of different conformational isomers within a single synthetic batch (or indeed as domains within a single particle) cannot be excluded as a possibility, and would significantly hinder the identification process from the convolution of Bragg peaks. In cases where single crystal diffraction (either X-ray or electron) is possible, identification could still be obstructed by twinning or solvation effects. Bulk crystals may contain different local regions consisting of these isomers, known as correlated disorder, wherein a spectrum of properties may be observed depending on said composition. Tuning correlated disorder has led to the potential of engineering the properties of MOFs.[57,58] For example, the existence of these previously unexamined isomers in MIL-53(X)-fum and potential correlated disorder may explain inconsistent adsorption behaviours and framework properties observed in previous studies.[48,59]

Prompted by our classification of the conformational isomers of MIL-53(X)-fum and characterisation of the third possible isomer, we investigate, herein, the effects of conformational isomerism, as well as the nature of the linking metal, on the extent of breathing in response to the presence and absence of pore-bound guests. Using *ab initio* molecular dynamics (AIMD), we study different metal homologues of the isomers, finding enhanced framework stability and rigidity that is unique to the Ga analogue of one isomer, MIL-53(Ga)-fum(*c*). To determine the caloric potential of MIL-53(Ga)-fum(*c*), we calculate the resulting adsorption-driven entropy change using grand canonical Monte Carlo (GCMC) simulations. Our work reveals a $\Delta S = 210(30)$ J K^{-1} kg^{-1} and 150(30) J K^{-1} kg^{-1} for $\Delta P = 0.4$ MPa with the adsorption of water and carbon dioxide, respectively. These quantities demonstrate that rigid MOFs are a promising potential class of refrigerants, with comparable performances and an improved efficiency over that of R-134a.

Methodology

The synthesis of MIL-53(In)-fum(*c*)

$In(NO_3)_3 \cdot xH_2O$ (0.0451 g, 0.15 mmol if $x = 0$) and fumaric acid (0.0172 g, 0.15 mmol) were dissolved in a mixture of *N*,*N*-dimethylformamide (DMF, 4 mL) and water (1 mL) in a 25 mL screw top glass jar. Concentrated HCl (37%, 50 μL, *ca* 0.60 mmol) was added and the jar was sealed. The clear solution was heated to 353 K in a programmable oven and kept at this temperature for 24 h to yield DMF solvated MIL-53(In)-fum(*c*) as colourless blocks. On cooling, an appropriate single crystal was selected for analysis directly from the reaction mixture without washing. The as-synthesised material was isolated by drying in a vacuum desiccator. Samples were activated by solvent exchange with acetone, followed by heating to 293 K for 24 h under 2×10^{-5} mbar vacuum.

The synthesis of MIL-53(Ga)-fum(*b*)

$Ga(NO_3)_3 \cdot xH_2O$ (0.0637 g, 0.25 mmol if $x = 0$) and fumaric acid (0.029 g, 0.25 mmol) were sonicated in DMF (10 mL) for 10 min. Concentrated HCl (37%, 20 μL, *ca* 0.25 mmol) was added and the mixture sealed in a Teflon-lined acid digestion vessel (Parr, 23 mL). After heating to 423 K in a programmable oven for 24 h, the mixture was cooled, and the solids isolated by centrifugation were washed three times with DMF (15 mL) before drying in a vacuum desiccator to yield the as-synthesised material. Samples were activated by solvent exchange with methanol, followed by heating to 293 K for 24 h under 2×10^{-5} mbar vacuum.

Single crystal X-ray diffraction

Ambient temperature single crystal X-ray diffraction (SCXRD) measurements were performed on the resulting MIL-53(In)-fum(*c*) crystals. A Bruker D8 VENTURE diffractometer equipped with a Bruker PHOTON II detector with Mo Kα radiation was used.[60] The SAINT routine implemented in the Bruker APEX3 software was employed for data integration.[60] SHELXL was used for the final structural refinements.[61,62]

Crystal data for MIL-53(In)-fum(*c*) ($C_7H_{10}InNO_6$, M = 318.98 g mol^{-1}): orthorhombic, space group *Pnma* (no. 62), a = 7.307(2) Å, b = 10.626(3) Å, c = 13.915(5) Å, V = 1080.4(6) Å^3, Z = 4, T = 298 K, μ(Mo Kα) = 2.196 mm^{-1}, D_{calc} = 1.961 g cm^{-3}, 5946 reflections measured (4.824° ≤ 2θ ≤ 52.89°), 1165 unique (R_{int} = 0.0511, R_{sigma} = 0.0420) which were used in all calculations. The final R_1 was 0.0362 ($I > 2\sigma(I)$) and wR_2 was 0.0876 (all data).

The crystal structure is available on the CCDC with the deposition number 2498629.

Powder X-ray diffraction

Powder X-ray diffractograms were collected using a benchtop Rigaku MiniFlex diffractometer at 298 K. Radiation was monochromated CuKα, with a characteristic wavelength of 1.5405 Å. Scans ranged from 3–45° and were collected on spinning zero-background holders. Selected diffractograms were fitted using Jana 2020.[63]

Thermogravimetric analysis

TGA measurements were carried out in air using a Discovery Series TGA 5500, with gas flows of 10 mL min^{-1} (balance) and 25 mL min^{-1} (sample). The analysis was completed with a heating rate of 10 K min^{-1} and a heating range of 298 K to 1073 K.

Gas adsorption analysis

N_2 adsorption–desorption isotherms (77 K, 0–1 bar) were carried out on activated samples using a Micromeritics 3Flex porosity analyser.

Density functional theory calculations and *ab initio* molecular dynamics

In order to accurately describe the organic–inorganic interactions within the system, a quantum mechanical based approach was taken and the system was simulated using the Quickstep module as implemented in the CP2K software package (version 2023.1).[64] The PBE function was chosen with Van der Waals corrections administered by Grimme's D3 corrections.[65,66] The atoms were described using the Goedecker-Teter-Hutter (GTH) pseudopotentials and a molecularly optimised double-zeta-valence-potential (DZVP-MOLOPT) basis set with a planewave cutoff energy of 750 Ry applied, in a periodic cell.[67]

It is known that the difference in metal centres can affect the flexibility and behaviours of MOFs with the MIL-53 topology.[68,69] To sample this, based on our solved solvated crystal structure of MIL-53(In)-fum(*c*) with DMF as the guest molecule, gallium and scandium analogues were derived computationally. This was accomplished by changing the "atom type" of the linking metal in the coordinates file. The framework was then vacated by removing the presence of guest atoms from the pores. This was repeated for MIL-53(X)-fum(*a*) and MIL-53(X)-fum(*b*), where the initial structures were obtained from previous published data.[48,50] Energy minimisation of the structures was achieved using the conjugated gradient (CG) method with a convergence criterion for changes in atomic position and forces as 0.003 Bohr and 0.003 Hartree/Bohr. A self-consistent field (SCF) was used with a convergence limit of 0.00001 Hartree.

Ab initio molecular dynamics (AIMD) simulations with the isobaric-isothermal ensemble (NPT) were used to simulate the systems at ambient pressure and temperature (0.1 MPa and 298 K). Velocity-rescaling was used for the thermostat and a barostat developed by G. J. Martyna *et al.* was employed with coupling parameters of 100 fs, post equilibration.[70,71] The systems were sampled with a timestep of 0.55 fs. To probe the thermal stability of the vacated system, subsequent simulations at ambient pressure (0.1 MPa) and temperatures of 400 to 650 K, in increments of 50 K, were performed. This range was determined from reported thermogravimetric analysis (TGA) measurements performed on MIL-53(Ga)-fum(*b*) which showed a decomposition temperature of near 673 K.[50] To access the closed structure of the frameworks and gauge the effect of the guest on the mechanical stability, the vacant systems were put under 100 MPa of pressure at 298 K.

By tracking how the potential energy varied with the volume of the system during the 100 MPa NPT simulation and binning the points based on volume, a potential energy surface (PES) was obtained. The bins were taken as constant intervals from the maximum to the minimum volume of the system, over the course of the simulation. The values in each bin were averaged and the uncertainty was taken as the standard deviation between the points in every bin. For the MD simulations at high pressures, the resulting PES would give information on the system properties at 100 MPa. The same method was used to generate a PES from the ambient MD outputs. However, as MIL-53(Ga)-fum(*c*) remains in the open phase, the comparable configurational space, defined by volume, was limited. To extrapolate and gain an understanding of how the potential energy surface would look when the system is not affected by pressure, configurations from each of the volume bins were taken from the high-pressure trajectory. Single point energy calculations were performed on the configurations. The uncertainty associated with each of the points were taken as the SCF convergence criteria. The results of this can be seen in Section 6 of the SI.

The porosities of the frameworks were analysed using the program PoreBlazer v4.0 which calculates the solvent accessible volume of the pores using either nitrogen atoms, helium atoms, or geometric grid estimations.[72] As with the GCMC simulations, the framework and nitrogen atom was described using the universal forcefield (UFF) parameters. The settings used can be found in Section 15 of the SI.

Grand canonical Monte Carlo

To probe the adsorption properties of the framework, a grand canonical Monte Carlo (GCMC) approach was used. Using the

RASPA2.0 code, 4 × 3 × 3 super cells of the DFT optimised frameworks were simulated and described using parameters from the Universal Force Field (UFF).[73,74] As physisorption was the predominant adsorption event, rather than chemisorption, the frameworks were simulated as a rigid body and the accuracy of the force field was deemed sufficient.[75–77]

Adsorbate molecules were given equal possibilities of insertion, deletion, rotation, and translation moves. The intermolecular interactions were modelled using Lennard-Jones (LJ) potentials with a coulombic term to describe the electrostatic contributions. The parameters for the water and carbon dioxide molecules were taken from the TIP5P force field and TraPPE force fields, respectively, chosen for their previous accuracies in predicting isotherms.[78–81] The full set of force field parameters was generated by a combination of the above parameters, using the Lorentz–Berthelot mixing rule.[82]

For each adsorbate, GCMC simulations with increasing external pressures of 1, 5, 10, 50, 100, 500, 1×10^3, 5×10^3, 1×10^4, 5×10^4, 1×10^5, 5×10^5, 1×10^6, 5×10^6, 1×10^7, 5×10^7, 1×10^8, 5×10^8, and 1×10^9 Pa were performed. For each pressure, around 400 000 post-equilibrated production MC steps were obtained. The radial distribution function (RDF) was calculated using the in-built RDF function from RASPA2.0 to give information on adsorption sites. The isosteric heat of adsorption (q_{is}) or the enthalpy of adsorption (ΔH_{ads}) was calculated from the GCMC outputs at every pressure using eqn (1).[83]

$$-\Delta H_{ads} = q_{is} = -\frac{\langle EN\rangle - \langle E\rangle\langle N\rangle}{\sigma(N)} + \mathrm{R}T \quad (1)$$

Where the angle brackets denote an average taken from every post-equilibration MC step, E is the total energy of the system, N is the number of guests adsorbed in the corresponding frame, $\sigma(N)$ is the variance of N across all of the steps, R is the gas constant, and T is the temperature of the system which had been set as 298 K for all of the simulations. Derived from fluctuation theory, the equation captures the variable number of particles during a GCMC simulation, wherein the numerator and denominator of the fraction represent the covariance between the energy and number of atoms, as well as the number of atoms with itself, respectively.[84] This equation holds in a single component system and is equivalent to the Clausius–Clapeyron equation in calculating q_{is}.[83] The resulting ΔH_{ads} represents the change in enthalpy with respect to the adsorption of a single guest molecule at a given pressure.[85] From this, the entropy change (ΔS_{ads}) associated with the adsorption event can be calculated as:

$$\Delta S_{ads} = \frac{\Delta H_{ads}}{T}. \quad (2)$$

To relate the entropy change (ΔS_{ads}) per adsorption event to the overall entropy change as a function of a change in pressure ($\Delta S_{ads}(\Delta P)$), the change in the number of guests corresponding to the pressure change ($\Delta N(\Delta P)$) must be considered. The $\Delta S_{ads}(\Delta P)$ values relate to the $\Delta N(\Delta P)$ through pressure. As such, the overall entropy change with respect to the change in pressure ($\Delta S_{tot,\Delta P}$) was derived from the area under the plot of $\Delta S_{ads}(\Delta P)$ against $\Delta N(\Delta P)$, see Section 11 of the SI. Between two adjacent data points on said plot, the entropy change ($\Delta S_{tot,P1\rightarrow P2}$) can be expressed as an integral of said plot, expressed as a function of $\Delta S_{ads}(\Delta P)$ and $\Delta N(\Delta P)$:

$$\Delta S_{tot,P_1\rightarrow P_2} = \int_{P_1}^{P_2} f(\Delta S_{ads}(\Delta P), N(\Delta P))\mathrm{d}N(\Delta P). \quad (3)$$

The implication of eqn (3) is that, there must exist a continuous function, $f(\Delta S_{ads}(\Delta P), N(\Delta P))$, between any given two points on a plot of $\Delta S_{ads}(\Delta P)$ against $\Delta N(\Delta P)$. In this work, a linear function was chosen to correlate $\Delta S_{ads}(\Delta P)$ and $\Delta N(\Delta P)$ between the two sampled pressure points (P_1 and P_2), *i.e.*,

$$f(\Delta S_{ads}(P_1,P_2), N(P_1,P_2)) = m_{\Delta S_{ads}(P_1,P_2),N(P_1,P_2)}N(P) + c_{\Delta S_{ads}(P_1,P_2),\,N(P_1,\,P_2)}, \quad (4)$$

where $m_{\Delta S_{ads}(P_1,P_2),N(P_1,P_2)}$ represents the gradient and $c_{\Delta S_{ads}(P_1,P_2),N(P_1,P_2)}$ is the y-intercept for the linear fit between the two points at different pressures. When integrated following eqn (4), by definition, the space between two pressure points is split into infinitesimally small steps. Hence, despite using a simple linear regression, the error of the fitting is minimised. To evaluate the integral and calculate $\Delta S_{tot,\Delta P}$ between two points, the trapezoidal rule was used. For changes in pressures that extend beyond two points, the resulting $\Delta S_{tot,\Delta P}$ was calculated as a summation of the integrals (see eqn. (3)) over the constituent pairs of pressure points, implemented using the chained trapezoidal rule.

The GCMC outputs used to compute the results shown, the analysis on the guest adsorption sites, and the full collection of ΔS_{tot} with respects to ΔP upon pressurisation/depressurisation are available in Sections 7–11 of the SI.

Results and discussion

Single crystal X-ray diffraction reveals the structure of MIL-53(In)-fum(*c*)

The crystal structure of MIL-53(In)-fum(*c*) was solved at 298 K using SCXRD. MIL-53(In)-fum(*c*) crystallises in the orthorhombic space group, *Pnma*, and has unit cell dimensions of $a = 7.307(2)$ Å, $b = 10.626(3)$ Å, and $c = 13.915(5)$ Å. In terms of metal-linker connectivity, the crystal structure of MIL-53(In)-fum(*c*) is analogous to the previously solved MIL-53 structures.[56,69,86] DMF molecules were located within the pores, hydrogen bonded to the μ_2-OH units through the formamide oxygen atom (O3···O4 = 2.750(10) Å). This hydrogen bond ensures the formamide oxygen atom (O4) is fully occupied in one position, while the remainder of the DMF molecule (other than the formamide nitrogen, N1) displays two-fold positional disorder. It is notable that the previously reported structures of MIL-53(X)-fum, which are reported as the (*a*) and (*b*) conformational isomers, all correspond to MOFs that had either been synthesised or worked up under aqueous conditions, suggesting a possible role of DMF in templating the formation of MIL-

53(X)-fum(*c*). The structure refinement parameters for MIL-53(In)-fum(*c*) can be found in Section 1 of the SI.

To our knowledge this is the first experimental characterisation of a MIL-53(X)-fum framework through SCXRD. As previously noted, when refining powder diffraction data, it may be possible to derive sensible structures corresponding to any of the predicted conformational isomers from the same diffractogram, depending on the method used. The significance of obtaining a structure by SCXRD is the fact that we can unequivocally confirm the existence of one specific isomer.

Enhanced rigidity and mechanical stability for MIL-53(Ga)-fum(*c*) over MIL-53(Ga)-fum(*a*) and MIL-53(Ga)-fum(*b*)

As discussed, conformational isomerism can have significant impact on the physical properties of MOFs.[52,54,55] Hence, in this work, we focus on simulating the different isomers by using a single unit cell which captures the inherent fumarate orientations of the MIL-53(X)-fum(*a*/*b*/*c*) structures that were experimentally obtained. Complementing the known isomers of MIL-53(Ga)-fum(*a*/*b*) studied by Ramaswamy *et al.* and Zhang *et al.*, by substituting Ga into our structure of MIL-53(In)-fum(*c*), we are able to complete the series of linker-orientational based conformational isomers for the MIL-53(Ga)-fum frameworks.[49,50] This enabled our investigation on the impact of the isomerism on the framework properties, as the only independent variable. This was achieved through AIMD NPT simulations at ambient (298 K and 0.1 MPa) as well as at elevated pressures of 100 MPa.

By simply tracking the evolution of the volume of the three systems in response to pressure, we are able to first qualitatively gauge the rigidity of the isomers when the pores are vacated of guest molecules. Of the three, we determine MIL-53(Ga)-fum(*b*) to be flexible, where the empty framework closes spontaneously under ambient temperature and pressure, with $\Delta V = \sim 50\%$ of the original unit cell. Previously, Zhang *et al.* concluded MIL-53(Ga)-fum(*b*) to be rigid after immersing the framework in different solvents and obtaining powder X-ray diffractograms, despite minor differences in the diffractograms of the as-synthesised and water hydrated materials.[50] This disparity in predicted flexibility could originate from uncertainty in the pore occupancy. As observed in other MOFs, including the MIL-53 family, it can be very difficult to confirm complete evacuation of guests, post synthesis or solvation.[87,88] Moreover, isomeric interconversion or coexistence in the bulk sample may occur.[89–91] Another important consideration when comparing experimental results to computational is the crystal size effect. Simulations employ periodic boundary condition which mimic crystalline systems with infinite unit cells. Meanwhile, in experimental settings, the crystal size is a variable that must be considered. For example, Johnson *et al.* demonstrated smaller crystals of ZIF-8 exhibited higher flexibility compared to the larger ones.[92]

As the aim is to minimise mechanical stress of refrigerants through framework rigidity, the predicted flexibility of completely evacuated MIL-53(Ga)-fum(*b*) was ill-suited for our application. Furthermore, as discussed, the opposing ΔS_{iso} from the ΔV to that of the corresponding adsorption event, would suggest that the flexible MIL-53(Ga)-fum(*b*) would have an inferior barocaloric potential compared to the two more rigid isomers.[44] On the other hand, we observed that both MIL-53(Ga)-fum(*a*) and MIL-53(Ga)-fum(*c*) remained in the open-phase at ambient conditions. While the results for MIL-53(Ga)-fum(*c*) have not been verified experimentally, the stability of the open MIL-53(Ga)-fum(*a*) framework agrees with the high-pressure powder X-ray diffraction experiments and calculated energy profile with respects to volume by Ramaswamy *et al.*[49] They determined the open phase of MIL-53(Ga)-fum(*a*) as the global minimum whereas the closed phase sits within a local minimum.

To gain further insight into the rigidity of the different isomers, we computed the energy of stabilisation which we define as the difference in potential energy (ΔE_{pot}) between the open and closed phases of each isomer. The larger ΔE_{pot} is, the more favourable it is for the framework to close. To attain the closed phases, we ran subsequent NPT simulations of the isomers with an increase in applied hydrostatic pressure of 100 MPa. Similar to the MIL-53(Al) framework, wherein the structural phase transition was characterised by a ΔV of ~40% combined with a reduction of the solvent accessible volume (SAV) from ~393 Å^3 to almost zero, we also observe a ΔV of ~50% with a change in SAV from ~550 Å^3 to 0 Å^3.[42] As such, we have characterised the observed structural change of the MIL-53(X)-fum(*a*/*b*/*c*) frameworks as a transition between different pore states, analogous to that observed in the MIL-53 frameworks. Between the pore states of the three isomers, we observed decreasing ΔE_{pot} in the order of (*b*) > (*a*) > (*c*), as detailed in Table S3 of the SI. The ΔE_{pot} for MIL-53(Ga)-fum(*b*) was the largest (−212.40(5) kJ mol^{-1}) which implied that it is the most favourable to close. This agrees with the more flexible nature of the structure as observed in the ambient NPT simulations. Additionally, the trend would imply that it is less favourable for isomer (*c*) to undergo the structural phase transition compared to (*a*), with ΔE_{pot} of −104.68(6) and −157.35(2) kJ mol^{-1}, respectively. Hence isomer (*c*) would possess a more rigid nature.

By constructing potential energy surfaces (PES) with respect to the volume of the framework, we are able to determine how much energy is required for the framework to transition from the open to closed phase. This potential energy difference allows us to indirectly probe the stability of the open-phase, and hence rigidity, of the MIL-53(Ga)-fum(*c*) isomer (see Fig. 3). At ambient conditions, we observe a single minimum at a volume of ~950 Å^3 which corresponds to the open phase. Fig. 3 infers a potential energy difference of 250 kJ mol^{-1} or greater for the system to transition towards the closed phase at 298 K and 0.1 MPa. In comparison, MIL-53(Ga)-fum(*a*) was previously calculated to have a ~15 kJ mol^{-1} difference.[49] The larger potential energy penalty infers that MIL-53(Ga)-fum(*c*) is more rigid than its isomeric counterpart with an open-phase that is more stable. At high pressures of 100 MPa, a large change in the potential energy surface was observed for MIL-53(Ga)-fum(*c*), clearly favouring the system in the closed phase (~580 Å^3), as one might expect.

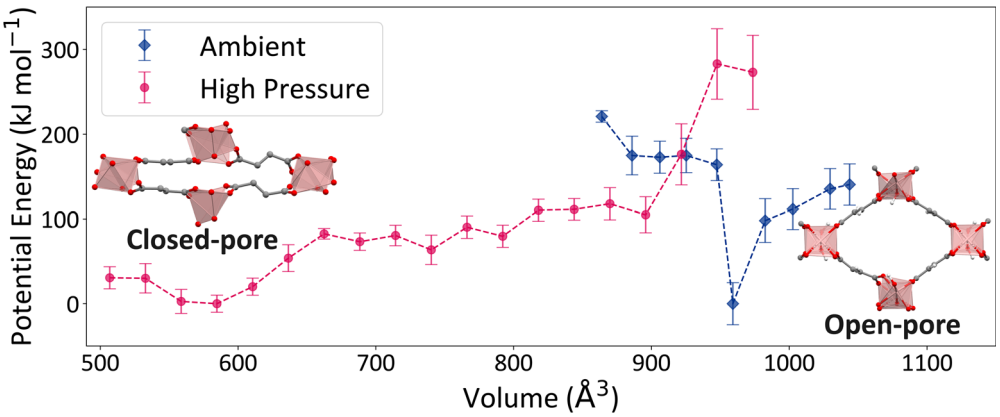

Fig. 3 Potential energy surface as a function of the unit cell volume for MIL-53(Ga)-fum(*c*), obtained from AIMD NPT simulations. Data was collected under ambient conditions (298 K, 0.1 MPa; blue diamonds) and high-pressure conditions (298 K, 100 MPa; pink circles). A clear shift in the global minimum is observed under elevated pressure. Error bars represent the standard deviation. The equilibrated structures of the open-pore and close-pore frameworks obtained from the ambient and high-pressure NPT simulations, respectively, are shown at the respective volume minima.

To understand whether MIL-53(Ga)-fum(*c*) and its rigidity can withstand operational temperatures, NPT simulations at increased temperature were conducted. For temperatures up to 650 K, we observed no closing of the framework. Unfortunately, all attempts to synthesise MIL-53(Ga)-fum(*c*) resulted in the isolation of the (*b*) conformational isomer (see Section 13 of the SI), with characterisation data closely related to that reported by Zhang *et al.*[50] The overall thermal stability predicted for MIL-53(Ga)-fum(*c*) is in good agreement with the TGA performed on MIL-53(Ga)-fum(*b*) by Zhang *et al.* and our own data (see Section 13 of the SI).[50] This implies that there is an insignificant effect on the chemical stability of the material associated with the inevitable warming and cooling of the material during a refrigerant cycle.[50] This sets MIL-53(Ga)-fum(*c*) apart from thermally activated frameworks such as MIL-53(Sc)-BDC which close upon heating.[41] As the recorded degradation temperature of the metal homologues of MIL-53-fum series exists within the range of 600 to 700 K, this family of framework can be regarded to possess good thermal stability.[50,93] The variability and trend of the degradation temperatures strongly suggest a metal-dependent thermal stability, with the Ga-based framework showing the higher stability amongst the metal homologues.

The differences in potential energy and rigidity between the three isomers, predicted in this work, highlights the importance of a robust characterisation method for MOFs with asymmetric linkers, like MIL-53(X)-fum. Depending on the intended application, one may find advantages in one isomer over the other, for example, the choice of rigid over a flexible framework in barocalorics. The combination of the thermal and mechanical stability of MIL-53(Ga)-fum(*c*) at ambient pressure (0.1 MPa) suggests the suitability of this framework as an adsorption-driven refrigerant that could overcome the challenge of mechanical failure during cyclic operation. Hence, we chose to continue the study with the MIL-53(Ga)-fum(*c*) isomer over MIL-53(Ga)-fum(*a*) or MIL-53(Ga)-fum(*b*), in this work.

The Ga analogues of MIL-53-fum(*c*) exhibit rigid properties over the flexible Sc and In analogues

To assess the effect of bridging metal on flexibility, we also probed the properties of the In and Sc homologues of the (*c*) isomer. The latter was achieved by substituting the In ions with Sc ions in the crystal structure of MIL-53(In)-fum(*c*). Unlike the more rigid Ga homologues, we find that both MIL-53(Sc)-fum(*c*) and MIL-53(In)-fum(*c*) frameworks transitioned towards the closed-phase with a smaller potential energy difference. This was statistically confirmed from 20 independent AIMD simulations initiated with random seeds with simulation lengths ranging from 4 ps to 8 ps. The simulation outputs of the metal homologues are shown in Section 3 of the SI. These simulations strongly indicate that the Ga ion was responsible for the observed rigidity of the MIL-53-fum(*c*) framework. The larger ionic radii of Sc^{3+} and In^{3+} compared to Ga^{3+} may be the reason for the metal-dependent flexibility, which would mirror that seen with MIL-53(X)-BDC series; MIL-53(Sc)-BDC adopts an extremely narrow pore form not seen in other homologues.[41,94] It was possible to scale up the synthesis of MIL-53(In)-fum(*c*) to collect bulk characterisation data (see Section 13 of the SI). After activation through solvent exchange in acetone and heating to 493 K for 24 under 2×10^{-5} vacuum, MIL-53(In)-fum(*c*) adopted a closed pore configuration. Le Bail fitting of powder X-ray diffraction data showed a unit cell volume of approximately 800 Å^3, and MIL-53(In)-fum(*c*) was non porous to N_2 (77 K, 1 bar) in contrast to the literature report of the rigidity and porosity of MIL-53(In)-fum(*b*).[50] These results further underpin the importance of conformational isomerism on the physical properties of MOFs, and validate the simulations.

Hence, Ga-based MIL-53-fum frameworks would be most applicable for minimising mechanical stress while maximising the performance during refrigeration cycles. The remainder of this paper aims to uncover the refrigeration capability of MIL-53(Ga)-fum(*c*).

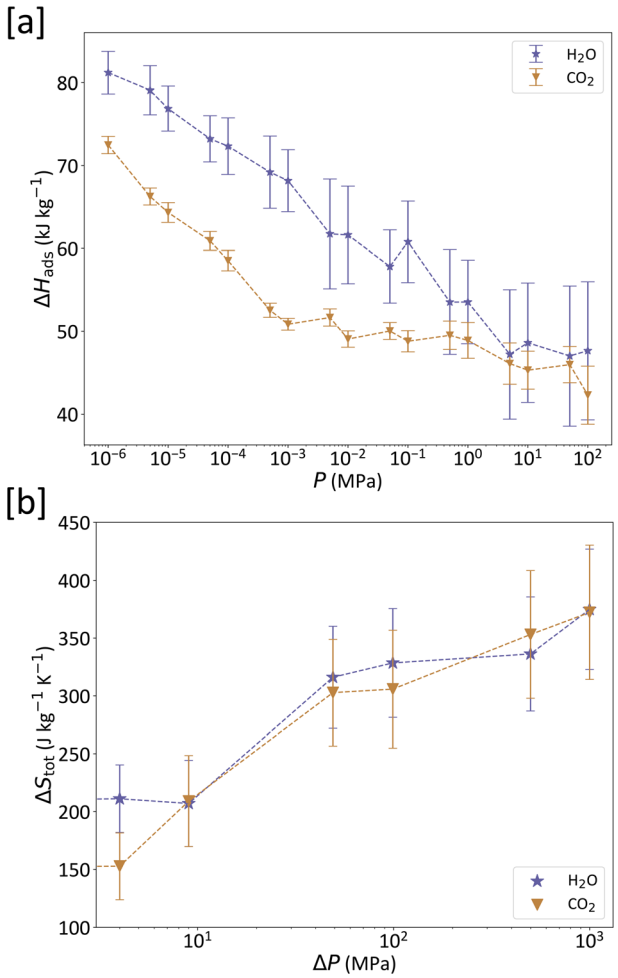

Fig. 4 Thermodynamic response of MIL-53(Ga)-fum(*c*) to external applied gaseous pressure. (a) Heat of adsorption as a function of external pressure for water and carbon dioxide, reported per kilogram of framework material. (b) Change in total entropy with increasing pressure for the adsorption of water and carbon dioxide, normalised per kilogram of MIL-53(Ga)-fum(*c*).

GCMC simulation can quantify adsorption-driven refrigeration potential of MIL-53(Ga)-fum(*c*) under low working pressures

As MIL-53(Ga)-fum(*c*) was determined to be rigid in nature at 0.1 MPa, GCMC simulations were performed to determine its adsorption driven refrigeration potential. The choice of water and carbon dioxide as adsorbates to drive the refrigeration process was motivated by green chemistry principals and safety concerns given the target application of refrigeration; both adsorbates are stable and do not have serious safety hazards associated with them. The simulated H_2O and CO_2 adsorption isotherms showed spontaneous adsorption of the guests into the pores at ambient conditions, in line with previous experimental work.[50] Notably, both adsorbate systems experience a large energetic stabilisation with the adsorption of guest molecules. Saturation of the framework occurred at 10 MPa, with ~16 water molecules or ~7 CO_2 molecules per unit cell. The difference in the number of molecules at saturation can be explained by the fact that CO_2 is a larger molecule and possesses rigid C=O double bonds which lead to less flexibility when it comes to packing compared to water. Furthermore, water can form hydrogen bonding networks that stabilise structures with higher loading. This is also observed in the calculated RDFs (see Section 9 of the SI).

The enthalpies of adsorption (ΔH_{ads}) for both adsorbates were determined across a pressure range of 1 Pa to 10 GPa, using eqn (1) (see Fig. 4a). ΔH_{ads} is a measure of the energy of stabilisation associated with the adsorption of one guest molecule in the framework. A clear decreasing trend was observed for the calculated ΔH_{ads} with increasing external pressure, as with many other systems.[9,95–98] At lower pressures, there are fewer guest molecules within the pores which results in less competition to the adsorption sites. At higher pressures, guest molecules compete, and increasing electrostatic repulsion leads to a destabilising effect which lowers the resulting ΔH_{ads}; this was also observed in the potential energy (see Fig. S16 and S17 in the SI). Overall, water exhibited a higher ΔH_{ads} compared to carbon dioxide which can be attributed to the stronger adsorbent–adsorbate interactions.

Comparing the calculated ΔH_{ads} values for CO_2 to the experimentally derived values for MIL-53(Al)-fum, our ΔH_{ads} values are greater by ~30 kJ mol^{-1} and ~10 kJ mol^{-1} at lower loading and as the framework reaches saturation, respectively.[99] The former implies stronger interactions between the Ga framework and the CO_2 molecules in comparison to the Al analogue. The inconsistent differences depending on loading are suggested to be artifacts of using a fully rigid framework in the GCMC simulations. Despite defining the MIL-53(Ga)-fum(*c*) as "rigid" in that the

Table 1 Comparison of entropy changes (ΔS) in response to pressure changes (ΔP) of: R-134a, the solid-state barocaloric neopentyl glycol (NPG), flexible breathing-caloric MOFs (MOF-508b and MIL-53(Al)-BDC), and the rigid MIL-53(Ga)-fum(*c*) shown in this work. *Change in pressure from ambient pressure (0.1 MPa)

Material	ΔS (J K^{-1} kg^{-1})	ΔP* (MPa)	Working mechanism	Reference
R-134a	~520	1.5	Barocaloric: vapour-compression	9
NPG	~510	570	Solid-state barocaloric: order–disorder transitions	11
MOF-508b	438.0	2.6	Breathing framework + CO_2 adsorption	21
MIL-53(Al)-BDC	311	1.6	Breathing framework + CO_2 adsorption	8
MIL-53(Ga)-fum(*c*)	210(30)	0.4	H_2O adsorption	This work
	−410(30)	−0.04		
	150(30)	0.4	CO_2 adsorption	This work
	−340(30)	−0.04		

framework does not close when vacated, local dynamics in the framework atoms and volume fluctuations can still occur (see Sections 3 and 4 of the SI). Research into comparing dynamic and static framework atoms has provided evidence to suggest that static adsorption simulations can overestimate adsorption in MIL-53(X) frameworks.[100] For water, our calculated ΔH_{ads} values are better matched to the experimental values; our values are greater by just ~10 kJ mol^{-1} and ~5 kJ mol^{-1} at lower to higher loading.[101] From the calculated RDFs, it is strongly implied that the predominant adsorption sites are either at the oxygen or hydrogen atoms of the framework (see Section 9 of the SI). Hence, we expect the ΔH_{ads} values between the Ga and Al analogues to be relatively comparable.

Using the chain trapezoidal rule, the change in entropy resulting from a change in pressure ($\Delta S_{tot,\Delta P}$) was calculated. From Fig. 4b, it can be inferred that, from an applied vapour pressure (ΔP) of 0.4 MPa from atmospheric pressure (0.1 MPa), the associated total entropy change (ΔS_{tot}) is 210(30) J K^{-1} kg^{-1} and 150(30) J K^{-1} kg^{-1} for water and carbon dioxide, respectively. While at the lowest pressure change, water performed better than carbon dioxide, the opposite was true for high pressure changes. Moreover, it was found that a negative ΔP from ambient pressures (shifting to sub-ambient pressures) results in a greater ΔS_{tot}. For $\Delta P = -0.04$ MPa, we calculate $\Delta S_{tot} = -410(40)$ and $-340(30)$ J K^{-1} kg^{-1} for H_2O and CO_2, respectively. At ambient pressure, both systems are already close to saturation hence, higher pressures were required for the adsorption of one more guest into the framework compared to lower pressures.

The roadmap of the Henry Royce Institute states that barocalorics should operate under pressures of 30 MPa to work efficiently and minimise energy consumption.[12] While questions on implementation are outwith the scope of this study, the colossal ΔS_{tot} in response to the low ΔP shown is competitive with the previously studied flexible MOFs and R-134a (see Table 1).[8,21] As such, we conclude MIL-53(Ga)-fum(*c*) to be good candidate as a green solid-state refrigerant.

Conclusions

We have identified and classified the different conformational isomers of the MIL-53(X)-fum frameworks based on the inherent orientation of the fumarate linkers. By conceiving a vector-based scheme which encodes information on the fumarate linker planarity and relative orientation, we have concluded that there are only three possible isomers based on the combinations of fumarate orientations. We have synthesised the novel MIL-53(In)-fum(*c*) framework material and, alongside the previous two reported isomers from the literature, completed the set of possible isomers. The importance of conformational isomerism is evident in AIMD simulations, which predict the open-phase of MIL-53(Ga)-fum(*c*) to be the most stable at ambient conditions, requiring more than 250 kJ mol^{-1} to transition towards the closed-phase, whilst MIL-53(Ga)-fum(*a*) and MIL-53(Ga)-fum(*b*) were either less stable in the open-phase or spontaneously closed under these simulated conditions. The stability of the unique rigid nature of the Ga homologue of the MIL-53(X)-fum(*c*) isomer against that of the In and Sc homologues was subsequently confirmed by further simulations. From this, we emphasise the need to consider these local isomeric structures and how they can significantly impact the properties of a framework. Our results indicate the need for single crystal structures (either from X-ray or electron diffraction) for MOFs with asymmetric linkers that can display such conformational isomerism.[102] The ability to unequivocally characterise the isomer(s) present allows for targeting specific isomers for their unique properties.

The enhanced thermal and mechanical properties present MIL-53(Ga)-fum(*c*) as a promising, long-lasting, and efficient refrigerant. The entropy change associated with adsorption was calculated to be 210(30) J K^{-1} kg^{-1} and 150(30) J K^{-1} kg^{-1} under 0.4 MPa of applied vapour pressure for water and carbon dioxide, respectively. These values are within the realms of colossal barocaloric materials and R-134a, which solidifies MIL-53(Ga)-fum(*c*) as a strong candidate for refrigeration applications. The implications of this work highlight the vast potentials in rigid MOFs, where the refrigeration efficiencies are improved while removing the problems associated with mechanical wear.

A sensible next step to this work would be to validate the results of this work with experimental adsorption isotherms and with thermal studies of the different isomers; this would require, however, an in-depth experimental study of the extent of isomerism and conversion within bulk samples, which cannot currently be captured by conventional powder diffraction methods. Our next work focusses on understanding interconversion pathways between the isomers to unlock the potential for property-driven framework engineering. To gain an insight into the correlated disorder and understand the extent of the tuneability of the framework as a result, supercell simulations would be required. More accurate force fields, perhaps in the form of a custom machine learning interatomic potential (MLIPs) which can also facilitate the study of the framework dynamics during adsorption cycles, may facilitate this computational work. Additionally, MLIPs can aid in the determination of a free energy surface to sample the open to closed phase transitions of these correlated disordered frameworks.[103–105] Our observations on the isomerism related to the fumarate linker may also help elucidate the behaviour of MOFs linked by other commonly used "stepped" dicarboxylate linkers, such as naphthalene-2,6-dicarboxylate, stilbene-4,4′-dicarboxylate, and azobenzene-4,4′-dicarboxylate, and further enhance the structural versatility amongst MOFs in these phase spaces.

Conflicts of interest

The authors declare no competing financial interest.

Data availability

CCDC 2498629 contains the supplementary crystallographic data for this paper.[106]

The data supporting this article have been included in the supplementary information (SI) and are available from the corresponding author upon reasonable request, provided that

the request is for legitimate academic or research purposes. The analysis codes used are open-source and available on the GitHub (https://github.com/hobdaylab/Codes_MIL-53-Ga-fum_paper). Supplementary information: SCXRD information and crystal structure for MIL-53(In)-fum(*c*), CCDC 2498629, outputs from AIMD and GCMC simulations, potential energy surfaces, RDF calculations, and entropy calculations. See DOI: https://doi.org/10.1039/d5ta08920d.

Acknowledgements

We acknowledge financial support from UK Research and Innovation (Future Leaders Fellowship MR/V026070/1 to C. L. H.) and the University of Edinburgh (Chancellor's Fellowship to C. L. H., doctoral studentships to C. C. H). R. S. F., W. L. L. and M. J. L. acknowledge support from the University of Glasgow and EPSRC (EP/T517896/1 and EP/W524359/1). This work used the Cirrus UK National Tier-2 HPC Service at EPCC (https://www.cirrus.ac.uk/) and ARCHER2 UK National Supercomputing Service (https://www.archer2.ac.uk/), funded by the University of Edinburgh and EPSRC (EP/P020267/1). Access to ARCHER2 was obtained *via* the UKCP consortium and funded by EPSRC grant ref (EP/X035891/1). This work has also made use of the resources provided by the Edinburgh Compute and Data Facility (ECDF) (https://information-services.ed.ac.uk/research-support/research-computing/ecdf), namely Eddie.

References

1 L. Wang, L. Wang, Y. Li and J. Wang, *Decis. Anal. J.*, 2023, **7**, 100237.
2 *Refrigerator Market Size, Share, Growth | Industry Trends*, 2032.
3 C. Cazorla, *Appl. Phys. Rev.*, 2019, **6**, 041316.
4 B. H. Samset, C. Zhou, J. S. Fuglestvedt, M. T. Lund, J. Marotzke and M. D. Zelinka, *Commun. Earth Environ.*, 2023, **4**, 400.
5 H. Hou, S. Qian and I. Takeuchi, *Nat. Rev. Mater.*, 2022, **7**, 633–652.
6 S. Crossley, N. D. Mathur and X. Moya, *AIP Adv.*, 2015, **5**, 067153.
7 X. Moya and N. D. Mathur, *Science*, 1979, **370**, 797–803.
8 J. García-Ben, J. López-Beceiro, R. Artiaga, J. Salgado-Beceiro, I. Delgado-Ferreiro, Y. V. Kolen'ko, S. Castro-García, M. A. Señarís-Rodríguez, M. Sánchez-Andújar and J. M. Bermúdez-García, *Chem. Mater.*, 2022, **34**, 3323–3332.
9 M. McLinden, in *ASHRAE Handbook*, ASHRAE, Atlanta, 2009.
10 B. Li, Y. Kawakita, S. Ohira-Kawamura, T. Sugahara, H. Wang, J. Wang, Y. Chen, S. I. Kawaguchi, S. Kawaguchi, K. Ohara, K. Li, D. Yu, R. Mole, T. Hattori, T. Kikuchi, S. Yano, Z. Zhang, Z. Zhang, W. Ren, S. Lin, O. Sakata, K. Nakajima and Z. Zhang, *Nature*, 2019, **567**, 506–510.
11 P. Lloveras, A. Aznar, M. Barrio, Ph. Negrier, C. Popescu, A. Planes, L. Mañosa, E. Stern-Taulats, A. Avramenko, N. D. Mathur, X. Moya and J.-L. Tamarit, *Nat. Commun.*, 2019, **10**, 1803.
12 J. Garcia-Ben, I. Delgado-Ferreiro, J. Salgado-Beceiro and J. M. Bermudez-Garcia, *Materials*, 2021, **14**, 5947.
13 P. Saikia, P. Gupta, T. R. Nath and N. K. Nath, *CrystEngComm*, 2024, **26**, 4259–4263.
14 K. Takazawa, J. Inoue, K. Mitsuishi, Y. Yoshida, H. Kishida, P. Tinnemans, H. Engelkamp and P. C. M. Christianen, *Sci. Rep.*, 2021, **11**, 3175.
15 V. Bon, N. Kavoosi, I. Senkovska and S. Kaskel, *ACS Appl. Mater. Interfaces*, 2015, **7**, 22292–22300.
16 J. M. Pringle, P. C. Howlett, D. R. MacFarlane and M. Forsyth, *J. Mater. Chem.*, 2010, **20**, 2056.
17 F. B. Li, M. Li, X. Xu, Z. C. Yang, H. Xu, C. K. Jia, K. Li, J. He, B. Li and H. Wang, *Nat. Commun.*, 2020, **11**, 4190.
18 J. Seo, J. D. Braun, V. M. Dev and J. A. Mason, *J. Am. Chem. Soc.*, 2022, **144**, 6493–6503.
19 A. Aznar, P. Lloveras, M. Romanini, M. Barrio, J.-L. Tamarit, C. Cazorla, D. Errandonea, N. D. Mathur, A. Planes, X. Moya and L. Mañosa, *Nat. Commun.*, 2017, **8**, 1851.
20 J. Seo, R. D. McGillicuddy, A. H. Slavney, S. Zhang, R. Ukani, A. A. Yakovenko, S.-L. Zheng and J. A. Mason, *Nat. Commun.*, 2022, **13**, 2536.
21 M. Gelpi, J. García-Ben, S. Rodríguez-Hermida, J. López-Beceiro, R. Artiaga, Á. Baaliña, M. Romero-Gómez, J. Romero-Gómez, S. Zaragoza, J. Salgado-Beceiro, J. Walker, C. J. McMonagle, S. Castro-García, M. Sánchez-Andújar, M. A. Señarís-Rodríguez and J. M. Bermúdez-García, *Adv. Mater.*, 2024, **36**, 2310499.
22 Z. Han, Y. Yang, J. Rushlow, J. Huo, Z. Liu, Y.-C. Hsu, R. Yin, M. Wang, R. Liang, K.-Y. Wang and H.-C. Zhou, *Chem. Soc. Rev.*, 2025, **54**, 367–395.
23 Z. Han, K.-Y. Wang, R.-R. Liang, Y. Guo, Y. Yang, M. Wang, Y. Mao, J. Huo, W. Shi and H.-C. Zhou, *J. Am. Chem. Soc.*, 2025, **147**, 3866–3873.
24 P. Deria, J. E. Mondloch, O. Karagiaridi, W. Bury, J. T. Hupp and O. K. Farha, *Chem. Soc. Rev.*, 2014, **43**, 5896–5912.
25 E. Martínez-Ahumada, M. L. Díaz-Ramírez, M. D. J. Velásquez-Hernández, V. Jancik and I. A. Ibarra, *Chem. Sci.*, 2021, **12**, 6772–6799.
26 J.-B. Lin, T. T. T. Nguyen, R. Vaidhyanathan, J. Burner, J. M. Taylor, H. Durekova, F. Akhtar, R. K. Mah, O. Ghaffari-Nik, S. Marx, N. Fylstra, S. S. Iremonger, K. W. Dawson, P. Sarkar, P. Hovington, A. Rajendran, T. K. Woo and G. K. H. Shimizu, *Science*, 1979, **374**, 1464–1469.
27 C.-H. Ho and F. Paesani, *ACS Appl. Mater. Interfaces*, 2023, **15**, 48287–48295.
28 W. Xu and O. M. Yaghi, *ACS Cent. Sci.*, 2020, **6**, 1348–1354.
29 I. Abánades Lázaro, X. Chen, M. Ding, A. Eskandari, D. Fairen-Jimenez, M. Giménez-Marqués, R. Gref, W. Lin, T. Luo and R. S. Forgan, *Nat. Rev. Methods Primers*, 2024, **4**, 42.
30 G. Liu, V. Chernikova, Y. Liu, K. Zhang, Y. Belmabkhout, O. Shekhah, C. Zhang, S. Yi, M. Eddaoudi and W. J. Koros, *Nat. Mater.*, 2018, **17**, 283–289.

31 C. E. Wilmer, O. K. Farha, Y.-S. Bae, J. T. Hupp and R. Q. Snurr, *Energy Environ. Sci.*, 2012, **5**, 9849.
32 D. Yang and B. C. Gates, *ACS Catal.*, 2019, **9**, 1779–1798.
33 L. Ma, C. Abney and W. Lin, *Chem. Soc. Rev.*, 2009, **38**, 1248.
34 V. F. Yusuf, N. I. Malek and S. K. Kailasa, *ACS Omega*, 2022, **7**, 44507–44531.
35 D.-W. Lim and H. Kitagawa, *Chem. Rev.*, 2020, **120**, 8416–8467.
36 C.-Y. Sun, X.-L. Wang, X. Zhang, C. Qin, P. Li, Z.-M. Su, D.-X. Zhu, G.-G. Shan, K.-Z. Shao, H. Wu and J. Li, *Nat. Commun.*, 2013, **4**, 2717.
37 Z. Liu, L. Zhang and D. Sun, *Chem. Commun.*, 2020, **56**, 9416–9432.
38 S. Seth and S. Jhulki, *Mater. Horiz.*, 2021, **8**, 700–727.
39 F. Formalik, A. V. Neimark, J. Rogacka, L. Firlej and B. Kuchta, *J. Colloid Interface Sci.*, 2020, **578**, 77–88.
40 M. Alhamami, H. Doan and C.-H. Cheng, *Materials*, 2014, **7**, 3198–3250.
41 L. Chen, J. P. S. Mowat, D. Fairen-Jimenez, C. A. Morrison, S. P. Thompson, P. A. Wright and T. Düren, *J. Am. Chem. Soc.*, 2013, **135**, 15763–15773.
42 Y. Liu, J.-H. Her, A. Dailly, A. J. Ramirez-Cuesta, D. A. Neumann and C. M. Brown, *J. Am. Chem. Soc.*, 2008, **130**, 11813–11818.
43 S. R. G. Balestra, R. Bueno-Perez, S. Hamad, D. Dubbeldam, A. R. Ruiz-Salvador and S. Calero, *J. Mater. Chem.*, 2016, **28**, 8296–8304.
44 W. K. Feldmann, C. Esterhuysen and L. J. Barbour, *ChemSusChem*, 2020, **13**, 5220–5223.
45 H. Liu, T. Fu and Y. Mao, *ACS Omega*, 2022, **7**, 14430–14456.
46 A. López-Olvera, J. A. Zárate, E. Martínez-Ahumada, D. Fan, M. L. Díaz-Ramírez, P. A. Sáenz-Cavazos, V. Martis, D. R. Williams, E. Sánchez-González, G. Maurin and I. A. Ibarra, *ACS Appl. Mater. Interfaces*, 2021, **13**, 39363–39370.
47 M. Gaab, N. Trukhan, S. Maurer, R. Gummaraju and U. Müller, *Microporous Mesoporous Mater.*, 2012, **157**, 131–136.
48 E. Alvarez, N. Guillou, C. Martineau, B. Bueken, B. Van de Voorde, C. Le Guillouzer, P. Fabry, F. Nouar, F. Taulelle, D. de Vos, J. Chang, K. H. Cho, N. Ramsahye, T. Devic, M. Daturi, G. Maurin and C. Serre, *Angew. Chem., Int. Ed.*, 2015, **54**, 3664–3668.
49 P. Ramaswamy, J. Wieme, E. Alvarez, L. Vanduyfhuys, J.-P. Itié, P. Fabry, V. Van Speybroeck, C. Serre, P. G. Yot and G. Maurin, *J. Mater. Chem. A*, 2017, **5**, 11047–11054.
50 Y. Zhang, B. E. G. Lucier, S. M. McKenzie, M. Arhangelskis, A. J. Morris, T. Friščić, J. W. Reid, V. V. Terskikh, M. Chen and Y. Huang, *ACS Appl. Mater. Interfaces*, 2018, **10**, 28582–28596.
51 T. Stassin, S. Waitschat, N. Heidenreich, H. Reinsch, F. Pluschkell, D. Kravchenko, J. Marreiros, I. Stassen, J. van Dinter, R. Verbeke, M. Dickmann, W. Egger, I. Vankelecom, D. De Vos, R. Ameloot and N. Stock, *Chem. – Eur. J.*, 2020, **26**, 10841–10848.
52 E. G. Meekel and A. L. Goodwin, *CrystEngComm*, 2021, **23**, 2915–2922.
53 P. St. Petkov, V. Bon, C. L. Hobday, A. B. Kuc, P. Melix, S. Kaskel, T. Düren and T. Heine, *Phys. Chem. Chem. Phys.*, 2019, **21**, 674–680.
54 E. G. Meekel, P. Partridge, R. A. I. Paraoan, J. J. B. Levinsky, B. Slater, C. L. Hobday and A. L. Goodwin, *Nat. Mater.*, 2024, **23**, 1245–1251.
55 S. Ehrling, E. M. Reynolds, V. Bon, I. Senkovska, T. E. Gorelik, J. D. Evans, M. Rauche, M. Mendt, M. S. Weiss, A. Pöppl, E. Brunner, U. Kaiser, A. L. Goodwin and S. Kaskel, *Nat. Chem.*, 2021, **13**, 568–574.
56 C. Serre, F. Millange, C. Thouvenot, M. Noguès, G. Marsolier, D. Louër and G. Férey, *J. Am. Chem. Soc.*, 2002, **124**, 13519–13526.
57 F. C. N. Firth, M. J. Cliffe, D. Vulpe, M. Aragones-Anglada, P. Z. Moghadam, D. Fairen-Jimenez, B. Slater and C. P. Grey, *J. Mater. Chem. A*, 2019, **7**, 7459–7469.
58 G. C. Shearer, S. Chavan, S. Bordiga, S. Svelle, U. Olsbye and K. P. Lillerud, *J. Mater. Chem.*, 2016, **28**, 3749–3761.
59 M. Froehly, G. Chaplais, H. Nouali, V. Roucoules and T. J. Daou, *New J. Chem.*, 2025, **49**, 5694–5706.
60 *APEX3, SAINT and SADABS*, Bruker AXS Inc., Madison, Wisconsin, USA, 2016.
61 G. M. Sheldrick, *Acta Crystallogr., Sect. C:Struct. Chem.*, 2015, **71**, 3–8.
62 G. M. Sheldrick, *Program for Crystal Structure Solution*, University of Göttingen, Göttingen, 2018.
63 V. Petříček, L. Palatinus, J. Plášil and M. Dušek, *Z. Kristallogr. Cryst. Mater.*, 2023, **238**, 271–282.
64 T. D. Kühne, M. Iannuzzi, M. Del Ben, V. V. Rybkin, P. Seewald, F. Stein, T. Laino, R. Z. Khaliullin, O. Schütt, F. Schiffmann, D. Golze, J. Wilhelm, S. Chulkov, M. H. Bani-Hashemian, V. Weber, U. Borštnik, M. Taillefumier, A. S. Jakobovits, A. Lazzaro, H. Pabst, T. Müller, R. Schade, M. Guidon, S. Andermatt, N. Holmberg, G. K. Schenter, A. Hehn, A. Bussy, F. Belleflamme, G. Tabacchi, A. Glöß, M. Lass, I. Bethune, C. J. Mundy, C. Plessl, M. Watkins, J. VandeVondele, M. Krack and J. Hutter, *J. Chem. Phys.*, 2020, **152**, 194103.
65 J. P. Perdew, K. Burke and M. Ernzerhof, *Phys. Rev. Lett.*, 1996, **77**, 3865–3868.
66 S. Grimme, J. Antony, S. Ehrlich and H. Krieg, *J. Chem. Phys.*, 2010, **132**(15), 154104.
67 J.-B. Lu, D. C. Cantu, M.-T. Nguyen, J. Li, V.-A. Glezakou and R. Rousseau, *J. Chem. Theory Comput.*, 2019, **15**, 5987–5997.
68 J.-P. Zhang, H.-L. Zhou, D.-D. Zhou, P.-Q. Liao and X.-M. Chen, *Natl. Sci. Rev.*, 2018, **5**, 907–919.
69 F. Millange and R. I. Walton, *Isr. J. Chem.*, 2018, **58**, 1019–1035.
70 G. Bussi, D. Donadio and M. Parrinello, *J. Chem. Phys.*, 2007, **126**, 014101.
71 G. J. Martyna, D. J. Tobias and M. L. Klein, *J. Chem. Phys.*, 1994, **101**, 4177–4189.
72 L. Sarkisov, R. Bueno-Perez, M. Sutharson and D. Fairen-Jimenez, *Chem. Mater.*, 2020, **32**, 9849–9867.
73 D. Dubbeldam, S. Calero, D. E. Ellis and R. Q. Snurr, *Mol. Simul.*, 2016, **42**, 81–101.

74 A. K. Rappe, C. J. Casewit, K. S. Colwell, W. A. Goddard and W. M. Skiff, *J. Am. Chem. Soc.*, 1992, **114**, 10024–10035.
75 Y. Sakanaka, S. Hiraide, I. Sugawara, H. Uematsu, S. Kawaguchi, M. T. Miyahara and S. Watanabe, *Nat. Commun.*, 2023, **14**, 6862.
76 M.-H. Lee, K. Vikrant, S. A. Younis, J. E. Szulejko and K.-H. Kim, *J. Clean. Prod.*, 2020, **250**, 119486.
77 Q. Liu, N. Hoefer, G. Berkbigler, Z. Cui, T. Liu, A. C. Co, D. W. McComb and C. R. Wade, *Inorg. Chem.*, 2022, **61**, 18710–18718.
78 D. D. Do and H. D. Do, *Colloids Surf. A Physicochem. Eng. Asp.*, 2006, **277**, 239–248.
79 M. W. Mahoney and W. L. Jorgensen, *J. Chem. Phys.*, 2000, **112**, 8910–8922.
80 S. W. Rick, *J. Chem. Phys.*, 2004, **120**, 6085–6093.
81 L. Zhang and J. I. Siepmann, *J. Phys. Chem. B*, 2005, **109**, 2911–2919.
82 H. A. Lorentz, *Ann. Phys.*, 1881, **248**, 127–136.
83 R. T. Cimino, P. Kowalczyk, P. I. Ravikovitch and A. V. Neimark, *Langmuir*, 2017, **33**, 1769–1779.
84 D. P. N. G. Nicholson, in *Computer Simulation and the Statistical Mechanics of Adsorption*, Academic Press Inc. Ltd, London, 1982, pp. 112–115.
85 W. J. Moore, in *Physical Chemistry* ed. W. J. Moore, Lowe & Brydone (Printers) Ltd, London, 1963, pp. 76–103.
86 A. U. Ortiz, A. Boutin, A. H. Fuchs and F.-X. Coudert, *J. Chem. Phys.*, 2013, **138**, 174703.
87 S. Leubner, R. Stäglich, J. Franke, J. Jacobsen, J. Gosch, R. Siegel, H. Reinsch, G. Maurin, J. Senker, P. G. Yot and N. Stock, *Chem. – Eur. J.*, 2020, **26**, 3877–3883.
88 J. R. H. Manning, G. Donval, M. Tolladay, T. L. Underwood, S. C. Parker and T. Düren, *J. Mater. Chem. A*, 2023, **11**, 25929–25937.
89 A. A. Kamin, E. J. Brannan, K. M. Snook, S. Krajewski, P. M. Gannon, W. Kaminsky and D. J. Xiao, *CrystEngComm*, 2024, **26**, 6396–6402.
90 H. H. Chen, S. Duan, Y. Sun, X. Song and J. Yu, *RSC Adv.*, 2020, **10**, 5604–5609.
91 H. Molavi and M. S. Salimi, *Sci. Rep.*, 2025, **15**, 7074.
92 L. J. W. Johnson, D. Mirani, A. Le Donne, L. Bartolomé, E. Amayuelas, G. A. López, G. Grancini, M. Carter, A. A. Yakovenko, B. A. Trump, S. Meloni, P. Zajdel and Y. Grosu, *Nano Lett.*, 2023, **23**, 10682–10686.
93 L. I. FitzGerald, A. L. Sutton, A. J. Seeber, B. W. Muir and C. M. Doherty, *ACS Omega*, 2025, **10**(18), 19206–19213.
94 F. Millange and R. I. Walton, *Isr. J. Chem.*, 2018, **58**, 1019–1035.
95 R. Oktavian, R. Goeminne, L. T. Glasby, P. Song, R. Huynh, O. T. Qazvini, O. Ghaffari-Nik, N. Masoumifard, J. L. Cordiner, P. Hovington, V. Van Speybroeck and P. Z. Moghadam, *Nat. Commun.*, 2024, **15**, 3898.
96 J. A. Mason, M. Veenstra and J. R. Long, *Chem. Sci.*, 2014, **5**, 32–51.
97 A. V. Palodkar, K. Anupam, Z. Roy, B. B. Saha and G. N. Halder, *Heat Mass Tran.*, 2017, **53**, 3155–3166.
98 H. Tun and C.-C. Chen, *Adsorption*, 2021, **27**, 979–989.
99 Z. Li, K. Shi, L. Zhai, Z. Wang, H. Wang, Y. Zhao and J. Wang, *Sep. Purif. Technol.*, 2023, **307**, 122725.
100 Z. Yu, D. M. Anstine, S. E. Boulfelfel, C. Gu, C. M. Colina and D. S. Sholl, *ACS Appl. Mater. Interfaces*, 2021, **13**, 61305–61315.
101 F. Jeremias, D. Fröhlich, C. Janiak and S. K. Henninger, *RSC Adv.*, 2014, **4**, 24073–24082.
102 R. J. Marshall, C. L. Hobday, C. F. Murphie, S. L. Griffin, C. A. Morrison, S. A. Moggach and R. S. Forgan, *J. Mater. Chem. A*, 2016, **4**, 6955–6963.
103 O. T. Unke, S. Chmiela, H. E. Sauceda, M. Gastegger, I. Poltavsky, K. T. Schütt, A. Tkatchenko and K.-R. Müller, *Chem. Rev.*, 2021, **121**, 10142–10186.
104 S. Vandenhaute, S. M. J. Rogge and V. Van Speybroeck, *Front. Chem.*, 2021, **9**, 718920.
105 A. Sharma and S. Sanvito, *npj Comput. Mater.*, 2024, **10**, 237.
106 CCDC 2498629: Experimental Crystal Structure Determination, 2022, DOI: 10.5517/ccdc.csd.cc2pw0yk.

